

Spatiotemporal Evolution of Marine Heatwaves Globally

H. A. Scannell¹, C. Cai², L. Thompson², D. B. Whitt³, D. J. Gagne³, R. P.
Abernathy¹

¹Jupiter Intelligence, Boulder, CO, USA

²School of Oceanography, University of Washington, Seattle, WA, USA

³National Center for Atmospheric Research, Boulder, CO, USA

Key Points:

- MHW objects are defined as spatially isolated areas of non-seasonal anomalous positive temperatures anomalies
- A MHW event is defined by one or more tracked objects allowing for space-time connectivity via objects that split and merge
- The largest MHW lasts from 2013 to 2018, encompassing the Northeast Pacific 2014-2015 event with a footprint throughout the Indo-Pacific Basin

Corresponding author: Cassia Cai, fmc2855@uw.edu

Abstract

The spatiotemporal evolution of marine heatwaves (MHWs) is explored using a tracking algorithm termed Ocetrac that provides objective characterization of MHW spatiotemporal evolution. Candidate MHW grid points are defined in detrended gridded sea temperature data using a seasonally varying temperature threshold. Identified MHW points are collected into spatially distinct objects using edge detection with weak sensitivity to edge detection and size threshold criteria. These MHW objects are followed in space and time while allowing objects to split and merge. Ocetrac is applied to monthly satellite sea surface temperature data from September 1981 through January 2021. The resulting MHWs are characterized by their intensity, duration, and total area covered. The global analysis shows that MHWs in the Gulf of Maine and Mediterranean Sea evolve within a relatively small region, while major MHWs in the Pacific and Indian Oceans are linked in space and time. The largest and most long lasting MHW using this method lasts for 60 months from November 2013 to October 2018, encompassing previously identified MHW events including those in the Northeast Pacific (2014-2015), the Tasman Sea (2015-2016, 2017-2018), and the Great Barrier Reef (2016).

Plain Language Summary

This study introduces a novel method, called Ocetrac, to track the spatiotemporal evolution of marine heatwaves (MHWs) using sea surface temperature data from 1981 to 2021. The method objectively identifies MHWs using temperature thresholds and edge detection, and then tracks them in space and time while allowing for splitting and merging. The resulting MHWs are characterized by intensity, duration, and total area covered. The study reveals that MHWs in the Gulf of Maine and Mediterranean Sea tend to evolve within a limited region, while major MHWs in the Pacific and Indian Oceans exhibit linked temporal evolution. The longest MHW identified using this method lasts for 60 months from 2013 to 2018, encompassing multiple previously identified MHW events.

1 Introduction

Marine heatwaves (MHWs) are defined as periods when the local sea surface temperature (SST) is significantly higher than typical for the time of year at a specified location. MHWs have occurred throughout the global ocean (Hobday et al., 2016; Holbrook et al., 2019). Typically, MHWs are examined through a local lens. Even when the drivers of marine heatwaves are well-known for a particular region (e.g., persistent anticyclonic atmospheric circulation over the North Pacific), the evolution of individual MHWs in these regions have varied considerably (Amaya et al., 2020; Bond et al., 2015; Fewings & Brown, 2019).

The motivation to understand the evolution of MHWs is owed to the vulnerability of marine ecosystems to temperature extremes (Smale et al., 2019). MHWs have led to mass mortalities in marine invertebrates (Oliver et al., 2017; Garrabou et al., 2009), species range shifts (Mills et al., 2013), habitat destruction including coral bleaching (Hughes et al., 2017), and harmful algal blooms (McCabe et al., 2016). Failure to anticipate the destructive impacts of MHWs leads to fishery management challenges, including changes to the supply chain and loss in value of commercially harvested species (Mills et al., 2013; Pershing et al., 2019; Cheung & Frölicher, 2020). Another potential concern is the impact of MHWs on regional atmospheric circulation that can perturb weather patterns over land, especially over densely populated regions. Such events have been associated with extreme drought leading to agricultural burdens (Williams et al., 2015; Rodriguez, 2021) and terrestrial heat extremes (McKinnon & Deser, 2018).

By definition, MHWs represent the extreme warm end distribution of local sea surface temperature anomalies. Previous studies have used the 90th (Oliver et al., 2018; Hob-

day et al., 2016) or 99th (Darmaraki et al., 2019; Frölicher et al., 2018) percentile of the SST distribution to define extremes, where a MHW event is identified when SST exceeds this threshold relative to a long-term fixed seasonal climatology for at least a certain period of time, e.g., 5-days; (Hobday et al., 2016). The distribution of MHWs is influenced by the mean state, natural variability, and long-term anthropogenic change (Frölicher et al., 2018; Oliver et al., 2018). Regions with large SST variance, for example in the vicinity of western boundary currents and their extensions, as well as in the equatorial Pacific cold tongue, have the highest MHW intensities globally (Oliver et al., 2018). In addition, Extremely long duration MHWs can be linked to modes of interannual to decadal variability in the climate system (Holbrook et al., 2019; Scannell et al., 2016).

Natural variability such as El Niño-Southern Oscillation (ENSO) can impact the presence and persistence of MHWs in the mid-latitudes through atmospheric teleconnections from the tropics. For example, anomalies in atmospheric deep convection over the tropics can initiate atmospheric planetary-scale waves that propagate to the mid-latitudes where they generate MHWs through changes in local atmospheric conditions, e.g., cloud cover (Hartmann, 2015). Large-scale modes of decadal SST variability that have been linked to tropical climate variability, such as the Interdecadal Pacific Oscillation (Power et al., 1999), can suppress or enhance the likelihood of MHW occurrences depending on the phase and amplitude of the mode (Holbrook et al., 2019; Scannell et al., 2016). They can influence the severity and duration of MHWs by altering the mean strength, direction, and location of ocean currents and heat transport, as well as modulate air-sea heat flux (Perkins-Kirkpatrick et al., 2019; Di Lorenzo & Mantua, 2016; Feng et al., 2013).

Interannual and decadal variability within the climate system can be explored using an empirical orthogonal function (EOF) decomposition of climate anomalies, with the first few EOF modes generally capturing enough of the variability to explain the dominant patterns of MHWs and their timescales (Di Lorenzo & Mantua, 2016). EOFs have been used to explain the spatial patterns and the long-lived persistence of prominent MHWs (Amaya et al., 2020; Fewings & Brown, 2019; Oliver et al., 2018; Di Lorenzo & Mantua, 2016). However, using a limited number of EOFs to describe the spatiotemporal evolution of MHWs gives an incomplete picture.

Retrospective and contemporaneous studies have relied on pointwise metrics (Sen Gupta et al., 2020; Hobday et al., 2018; Oliver et al., 2018), fixed region heat budget analyses (Xu et al., 2018; Oliver et al., 2017; Bond et al., 2015; Chen et al., 2014), or EOFs (Di Lorenzo & Mantua, 2016) to characterize the drivers of specific MHW events and to describe their characteristics. These approaches have been widely successful in determining the local processes and remote drivers responsible for specific MHWs (Sun et al., 2023). Here, we expand this view by characterizing the spatiotemporal evolution of MHWs as they evolve globally. This new perspective of MHW evolution takes advantage of the 3D evolving field of global SST to detect and track MHWs by characterizing their shape, size, location, duration, and intensity, which may help to identify new patterns in how MHWs evolve. We use an object-tracking algorithm, called Ocetrac, to explore the large-scale spatial connectivity of MHWs as they evolve in time and describe events as connected components.

Object tracking has been used in atmospheric sciences of atmospheric and oceanic phenomena. For instance, an enhanced watershed method was used to identify hailstorm objects using observed gridded radar reflectivity and column integrated graupel mass estimates from a National Weather Prediction (NWP) model (Gagne et al., 2017). The enhanced watershed method (Lakshmanan et al., 2009) reduces the volume of data that needs to be processed by optimally searching for the local maxima in the storm field and growing the storm object until both area and intensity criteria are met. As with Ocetrac, the watershed object-identification method is parameter sensitive.

The analysis presented here allows an investigation into the spatiotemporal evolution of MHWs. We use several definitions in our analysis (Table 1). Features are individual points where SST is above the locally defined threshold for one month. A MHW object is a spatially coherent collection of features. A MHW event is composed of tracked and linked objects. We apply Ocetrac to monthly SST data from 1981 through 2021 to track the evolution of all MHWs globally and examine the distribution of three key MHW metrics (size, intensity, and duration). Four unique MHW case studies are further explored using this framework in the North Pacific, North Atlantic, Indian Ocean, and Mediterranean Sea.

2 Methods

2.1 Data and Preprocessing

We analyze monthly global maps of SST from the 0.25° longitude by 0.25° latitude gridded Optimum Interpolation SST version 2.1 (OISSTv2.1) dataset that extends from September 1981 through January 2021. The OISSTv2.1 combines satellite Advanced Very High Resolution Radiometer (AVHRR-only) with observations from ship, buoy, and in-situ measurements (including Argo floats and drifters), while accounting for platform differences and using interpolations to fill gaps in the satellite data (Reynolds et al., 2002, 2007). We create a mask over the Arctic ($>65^\circ\text{N}$) and Antarctic ($>70^\circ\text{S}$) Oceans to remove data in these regions and to avoid influence from seasonal sea ice and where the OISSTv2.1 data are less reliable (Figure 1).

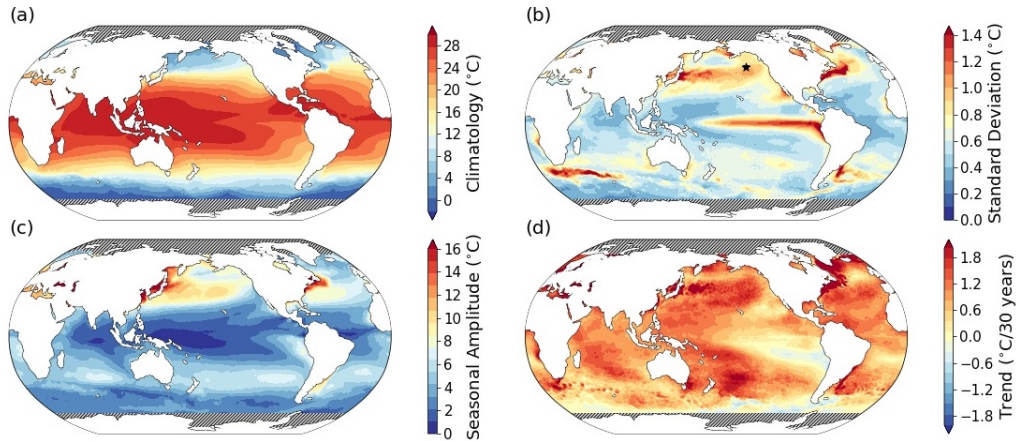


Figure 1. Global distribution of (a) mean SST (SST_m), (b) standard deviation of the anomalies detrended (SST_a), (c) amplitude of the seasonal cycle (SST_s) as the peak minus the trough, and (d) 30-year trend (SST_t) from 1990 through 2020. Maps in (a-c) have means computed with respect to September 1981 through January 2021. Hatching over the polar oceans represent regions that are excluded from this analysis.

Using the global maps of SST, we remove the mean, linear trend, and seasonal cycle from September 1981 through January 2021 to compute anomalies. The total decomposition of monthly SST is represented as

$$SST_{fit} = SST_m + SST_s + SST_t \quad (1)$$

where the fit (SST_{fit}) is the linear combination of the mean (SST_m , Figure 1a), linear trend (SST_t), annual and semiannual harmonics (SST_s) at each grid point. The coefficients of SST_{fit} are found using the least squares regression fit to monthly SST computed over the 473-month time period. We define detrended SST anomalies SST_a as the standardized difference between monthly SST and SST_{fit} , such that

$$SST_a = SST - SST_{fit} \quad (2)$$

Our analysis is performed on SST_a to allow us to focus on the processes that underlay the evolution of MHWs. If the long-term trend is not removed, towards the end of the record, most of the global ocean is in MHW conditions year round. The trend is largest in mid-latitudes in the subtropical gyres, especially in the Northwest Atlantic, western North Pacific, and western South Pacific. This allows an examination the evolution of the spatial characteristics of MHW evolution (Figure 1d).

We standardize SST_a by dividing by the respective local monthly standard deviation of SST_a over the entire period. The resulting standardized anomaly fields (SST_a^*) have uniform variance across the globe. Equal variance of SST_a^* accounts for non-seasonal spatial variability in the magnitude of SST_a that is shown in Figure 1b. High standard deviations of SST_a^* occur in the eastern equatorial Pacific, western boundary currents, the region connecting the Indian Ocean to the South Atlantic, and in frontal zones with large SST gradients. Comparatively, the subtropics, southern mid-latitudes, equatorial Atlantic Ocean, equatorial Indian Ocean, and western tropical Pacific have low standard deviations (Figure 1b).

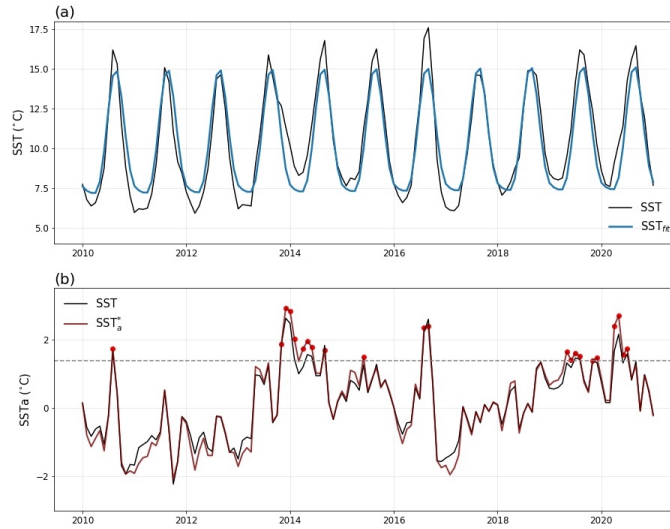


Figure 2. Monthly time series of (a) SST and (b) SST_a from January 2010 through January 2021 at 46.625°S, 148.875°W (star in Figure 1b). The mean, seasonal cycle, and trend in SST are shown in (a) as SST_{fit} . SST_a in (b) is defined as SST minus SST_{fit} . The standardized SST_a^* is shown in red and has been divided by its monthly standard deviation. Red circles indicate when the SST_a^* exceeded the 90th percentile of SST_a^* (shown by the dashed line) computed over the entire period from September 1981 through January 2021.

2.2 Anomaly Detection

To identify MHWs from the monthly maps of SST_a^* , we search for candidate MHW points when the SST_a exceeds an intensity threshold defined as the local seasonally varying 90th percentile of SST_a at each grid point and for each month (as suggested in Hobday et al., 2015). If we apply the same procedure with $SST - SST_t$, the results will be the same because $SST_m + SST_s$ is a constant for each grid point and month of the year. When the SST_a exceeds the threshold, we consider it a MHW candidate.

2.3 Multiple Object Tracking

The standardized SST_a maps with the MHW candidate points produced by the anomaly detection algorithm in Section 2.2 are transformed into a binary image where ones correspond to candidate MHW grid points and zeros correspond to background grid points. Each monthly map is treated as a separate image. Our goal is to identify groupings of ones that define a MHW object, which meet the defined spatial characteristics in terms of structure and size. Image processing terminology is defined in Table 1 and illustrated in Figure 3.

Table 1. Glossary of terms used in image processing and set theory.

Term	Definition
Binary Image	A 2D map (x, y) with ones corresponding to candidate MHW grid points and zeros corresponding to either non-MHW grid points or land points.
Features	Within binary images, features refer to grid points with values of one.
Objects	Within binary images, clusters are features that are connected in either space or time (x, y, t) .
Structuring Element	A 2D binary image with unique shape and size applied in the morphological operations such as erosion and dilation.
Connectivity Element	Centrosymmetric 3D binary array to track MHWs in space and time (x, y, t) .
Erosion	Contracts the boundary of a binary image and removes small-scale details.
Dilation	Expands the boundary of a binary image by adding a layer of pixels.
Opening	Erosion followed by dilation. Smooths contours by breaking narrow isthmuses: eliminates small islands and sharp peaks.
Closing	Dilation followed by erosion. Smooths contours by fusing narrow breaks and long thin gulfs: eliminates small holes.
Centroid	The geographic center of each object. A MHW can have multiple centroids if connected objects merge or split.
Sub ID	An additional ID given to MHWs with more than one centroid per month. For example, the 50th MHW with three centroids would be labeled as 50.1, 50.2 and 50.3 respectively.

We use mathematical morphology operations from the SciPy multidimensional image processing Python package to remove small, isolated features and to fill small holes within feature clusters. A structuring element is defined according to its shape and size.

We define the shape of the structuring element (S) by a quadratic surface with a morphological radius (R), where

$$S = x^2 + y^2 \quad (3)$$

Here, x and y are vectors with length $2R$ and represent longitude and latitude coordinates. The matrix, S , is transformed into a binary image and is represented by ones where $S < R^2$ is satisfied, otherwise the background is zeros (Figure 3). The units of S are in degrees per unit resolution of the grid (e.g., an R of 8 on a $1/4^\circ$ grid is equal to 2° latitude or longitude). We iterate through different values of R to explore how the size of the structuring element affects MHW characteristics. By design, S represents a subset of the binary image with a defined structure and is used to scan over the MHW image during morphological opening and closing.

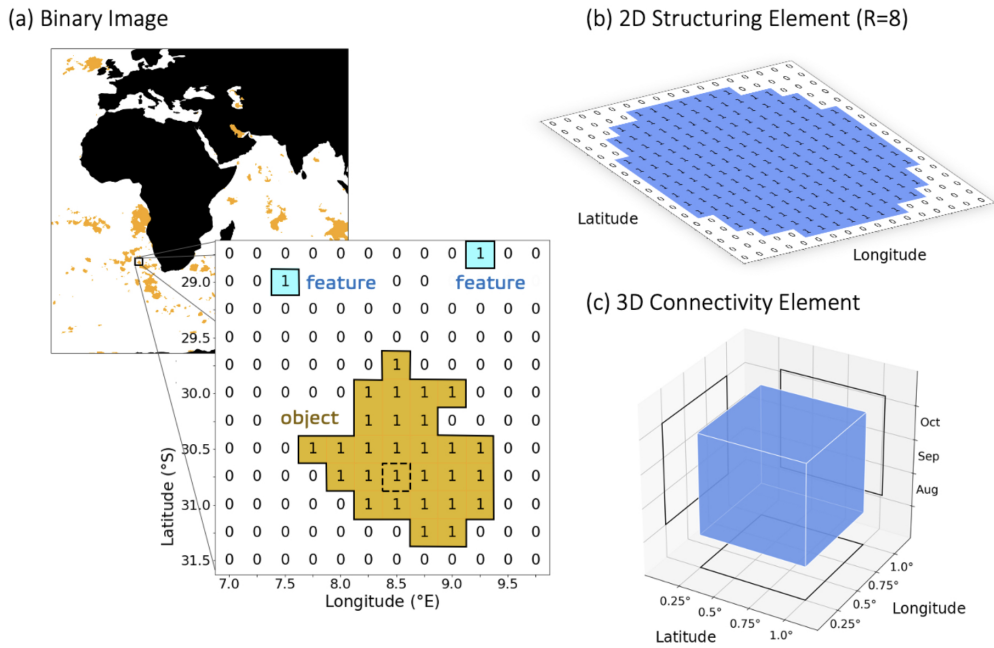


Figure 3. Illustrations of terminology used in Ocetrac. The (a) binary image contains features and connected features called objects. The centroid of an object is defined by its geometric center (dashed grid box in (a)). A (b) 2D structuring element is used in morphological operations with $R=8$, and a (c) 3D connectivity element is used in multiple object tracking.

The structuring element is used to scan over the entire image to manipulate features based on the dilation and erosion of the image (Gonzalez & Woods, 2002). Erosion eliminates isolated and small features by shrinking features. Dilation is the opposite of erosion and is used to fill small holes within features, gradually enlarging the boundaries of the feature region.

Erosion and dilation are done for each unique positional element in the image, and their operations are performed in succession (Figure 4). For example, morphological opening is erosion followed by dilation using the same structuring element. Opening is used to eliminate small features while preserving the shape and size of larger features in the image. Alternatively, morphological closing is the process of eroding a dilated image, again

using the identical structuring elements used in the opening procedure. Closing fills small holes within features while also preserving the shape and size of other features in the image. Both opening and closing are used to remove small features and smooth the borders of larger features. Here, we implement a series of morphological closing then opening, as we found this to optimally clean feature images that can be tracked in space and time (Figure 4).

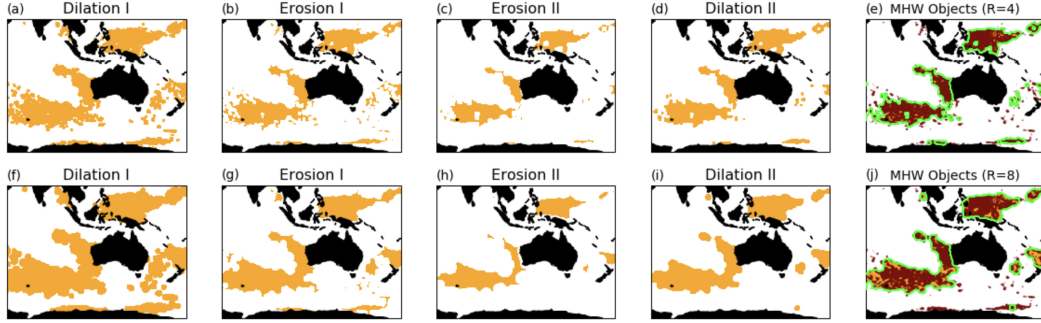


Figure 4. Sequence of morphological operations for closing (Dilation I followed by Erosion I) then opening (Erosion II followed by Dilation II) using a structuring element with a radius of 4 grid cells (a-e) and a radius of 8 grid cells (f-j). Orange shading represents the feature area that the morphological operations are performed on. Red stippling in (e, j) shows the grid cells identified as potential MHWs before the morphological operations. Green contours outline the final shape of the identified MHW objects. Data shown here is from February 2011 using the $1/4^\circ$ resolution OISSTv2 $SSTa^*$ with the trend removed and 90th percentile as the threshold for anomaly detection.

Next, we label connected 2D objects from binary images using Scikit-Image’s measure module in Python. We define objects when two or more neighboring features with the same value are connected either adjacent or diagonal from each other (e.g., orange pixels in Figure 3a). The resulting 2D objects are assigned a unique label. This process is repeated for each time step. For each unique object, we use the latitude and longitude coordinates from the Scikit-Image’s regionprops module to calculate total object area. Using the distribution of all object areas from September 1981 through January 2021, we calculate the area at a particular percentile threshold (P) and ignore objects smaller than P . For our purposes, we use the 75th percentile of object area (km^2) for the value of P (Figure 4). We discuss the sensitivity of the chosen size threshold on MHW characteristics in Section 3.

After eliminating objects smaller than the size threshold, we convert the images back to binary where ones correspond to objects and zeros are considered the background. We redefine objects using a 3D centrosymmetric connectivity element, such that two features with similar values that are either adjacent or diagonal to each other and that also overlap in time are connected. Objects are again uniquely labeled with an ID and tracked sequentially through time. No temporal gaps are allowed and no minimum percent overlap is enforced. We allow multiple objects that merge to have same ID and a single object that splits into multiple objects that retain the ID of the initial object. As a result, any objects that have connectivity at some point in their evolution share an ID. This allows MHWs to contain multiple objects.

In summary, we describe a new tracking algorithm to detect and follow the evolution of MHWs. The results depend on the morphological radius (R) and minimum size

percentile threshold (P). We discuss the sensitivities of these choices in Section 3, along with useful metrics for characterizing the global spatiotemporal evolution of MHWs.

3 Sensitivity Analysis

The representation of MHWs is dependent on the criteria used to define their intensity, size, duration, and shape. This can be influenced by the horizontal resolution of the SST data, and whether or not the trend is removed. We investigate the sensitivity of the morphological radius (R) and minimum size percentile threshold (P) criteria implemented in Ocetrac. Specifically, we quantify the effect of these criteria on the number of MHW events detected, average MHW duration, minimum MHW area, and the percent of MHWs with multiple centroids.

As R and P increase, fewer MHWs are detected (Figure 5a). Large values of R increase the connectedness of features in the binary images, resulting in fewer but larger MHW events. These well connected MHWs are also likely to persist for longer than 3 months (Figure 5e). The percentage of MHWs with multiple centroids decreases with increasing R (Figure 5d). Fewer MHWs have multiple centroids when R is large as a result of increased connectivity among features.

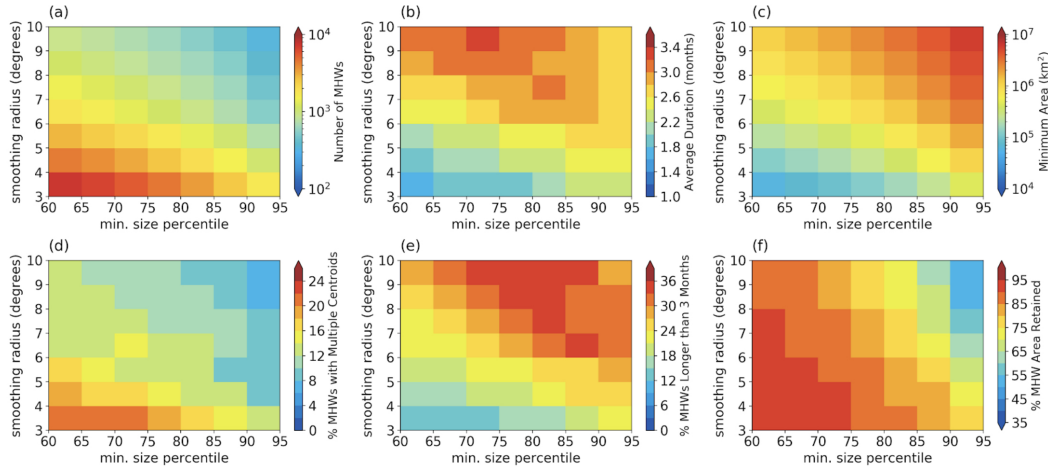


Figure 5. Sensitivity of MHW characteristics globally with varying smoothing radius (R) and minimum size percentile (P), including the (a) number the MHWs detected from September 1981 through April 2020, (b) average monthly duration of MHWs, (c) minimum MHW area, (d) percent of MHWs with multiple centroids, (e) percent of MHWs longer than 3 months, and (f) percent of MHW area retained. Data shown here are for $1/4^\circ$ resolution OISSTv2 with MHWs defined when detrended SST exceeds the local monthly 90th percentile from September 1981 through April 2020.

The average monthly duration of MHWs initially increases with R and P for values of $P < 70$ (Figure 5b); however, for large R , the average monthly duration peaks for R near 75. This nonlinear behavior is the result of the decline in the number of MHWs detected as the minimum size percentile increases. A smaller population size decreases the average duration (Figure 5b and e). Duration appears most sensitive to smoothing radius, where large radii increases connectivity between neighboring features allowing MHWs to persist for longer periods of time.

Large minimum thresholds P reduce the percentage of the total MHW area retained. Smaller values of P thresholds retain a greater percent of the original MHW area, and therefore also produce more MHWs of smaller size (Figure 5a, c, and f). As the size threshold increases, the percent of total MHW area retained quickly declines to less than 50% (Figure 5f). The number of MHWs detected also declines to less than 100 with the smallest size events increasing in size. If the size threshold R is held constant, the percent of total MHW area retained also decreases and the minimum MHW area increases with increasing smoothing radius. The larger smoothing radii help join neighboring features and fill holes within feature clusters. Thus, a large smoothing radii help to grow MHWs, while also decreasing the total number of MHWs detected.

For a demonstration of the sensitivity of an example MHW to the smoothing radius and size percentile threshold, we examine the sensitivity of the 2011 MHW off Western Australia (Figure 6). The shape and size of the detected objects are noticeably different between radii of 4 and 8, and the results are independent of area threshold P . A smoothing radius of 4 produces objects with sharp and jagged edges and interior holes (Figure 6a, d, and g). The object shape difference between an R of 8 and 10 is nearly negligible, with the exception of small features disappearing (e.g., Figure 6b vs. Figure 6c). As the minimum size threshold P increases, objects disappear when the areas fall below the threshold. The sensitivities of the radius and size parameters give insight into the biases introduced in tracking MHWs. Here, we use a radius of 8 as it provides enough detail of the original objects while creating smooth edges. We also choose the 75th percentile for the minimum size threshold as it isolates the well-known MHWs that have occurred in the 21st century, including the event of Western Australia in 2011 (Figure 6e).

The sensitivity analysis reveals the effect that the choice of parameter influences basic characteristics of MHWs such as number, duration, and size. To optimize our choice, we aim for approximately 20 MHWs per year (approx. 800 from 1982 to 2020), a minimum area roughly the size of Alaska (approximately $2 \times 10^6 \text{ km}^2$), and lasting on average 3 months (Holbrook et al., 2019).

4 Metrics

Ocetrac allows for the characterization of discrete MHWs in time and space. We define a set of measures that are computed over the lifetime of each event and at monthly increments (Table 1). To describe the intensity within the MHW, we use the entire SSTa field within the object contour (green outlines in Figure 6) to calculate the mean, maximum, and cumulative intensity. These quantities are calculated with respect to the local monthly climatology from 1982-2020 that have been standardized by the local monthly standard deviation of the SSTa*. The MHW anomalies are summed over the area and duration of the event to calculate the cumulative intensity. Degree heating weeks ($^{\circ}\text{C}$ -weeks) are commonly used to study the impacts of coral bleaching in tropical reef ecosystems (Kayanne, 2017; Eakin et al., 2010). The cumulative intensity ($^{\circ}\text{C}\text{-km}^2$ -months) provides a measure of accumulated heating over the lifetime of the MHW and can be informative when assessing the time, space, and temperature dependence of ecological impacts related to MHWs.

MHWs have a discrete start and end date that define the event duration. The start date is determined once the SSTa is exceeds the local 90th percentile with a continuous area exceeding the minimum size threshold as defined by P . The termination of a MHW occurs when either the SST falls below the temperature threshold as defined by P or when the area diminishes to less than the minimum size as defined by P . The sampling frequency is monthly. Events with durations shorter than a month are not considered.

Area is an important qualifier for a MHW. The area is defined as the sum of grid boxes contained within each object and takes into consideration grid resolution and lat-

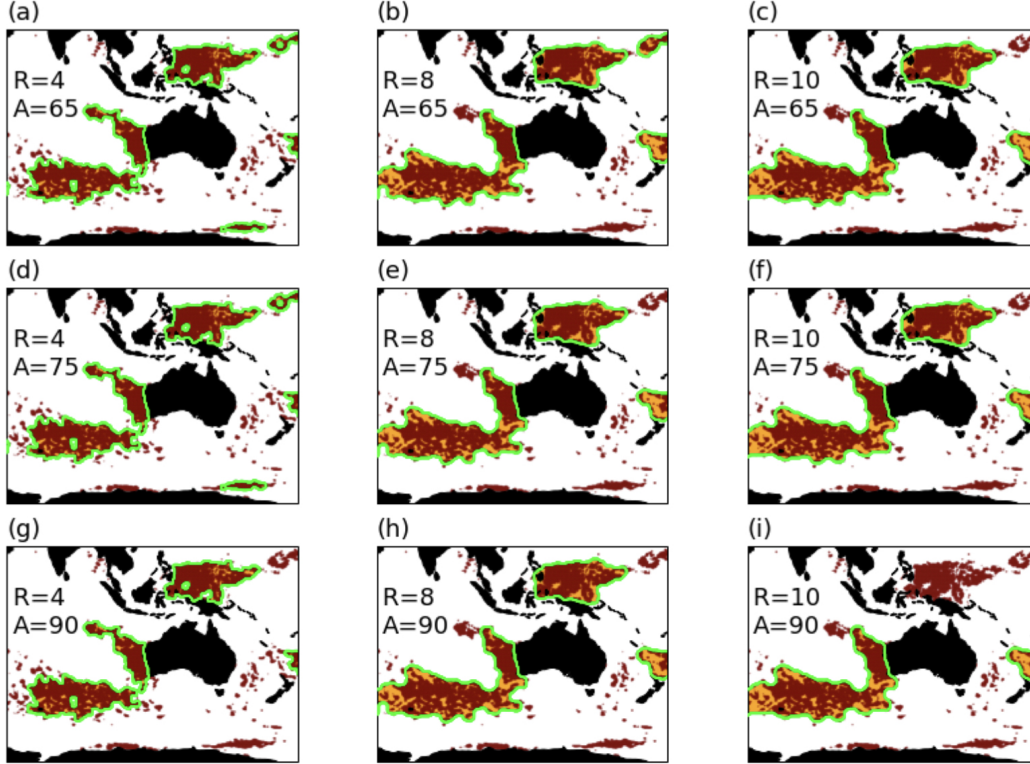


Figure 6. Sensitivity of objects detected from the morphological operations in February 2011 from the $1/4^\circ$ resolution OISSTv2 with the trend removed and 90th percentile as the threshold for anomaly detection. Each panel represents a unique combination of radius and minimum size threshold from 4–10 grid spaces and 65th–90th percentiles respectively. Detected objects are outlined in green, red stippling indicates grid points where SST exceeds the 90th percentile, and orange shading represents filled in MHW regions to create closed contour objects outlined in green.

Table 2. Description of measures used to characterize individual MHW events.

Term	Definition	Definition
Intensity		
Mean	$^\circ\text{C}$	Average SSTa
Maximum	$^\circ\text{C}$	Maximum SSTa
Cumulative	$^\circ\text{C km}^2$ months	Sum of SSTa over the total area for the duration of the event
Duration	months	Persistence of MHWs in time
Area		
Mean	km^2	Average MHW grid area over the duration of the event
Maximum	km^2	Largest MHW grid area over the duration of the event
Cumulative	km^2	Sum of unique grid area over the duration of the event
Centroid	($^\circ\text{lat}$, $^\circ\text{lon}$)	Geometric center of each object for each MHW defined at each time step

itude. Since MHW with multiple objects can contain several centroids, we also compute the area for each object within the MHW. Given that MHWs evolve in space over their lifetime, it is informative to find the total MHW area as the sum of unique grid points contained within the MHW over its duration. The mean and maximum areas are computed for each MHW.

The distributions of MHW duration and area are heavy-tailed, meaning that short lived or small area events occur more frequently than long-lasting or large area events (Figure 7). By construction, both duration and area have minimum thresholds of one month and $1.85 \times 10^6 \text{ km}^2$ respectively. The largest MHW encompassed the 2013-2017 NE Pacific "The Blob," impacting a total area of $2.88 \times 10^{10} \text{ km}^2$ and persisting for 60 months. The MHW off Western Australia a total area and duration covering $1.62 \times 10^{10} \text{ km}^2$ for 47 months (Table 3). The Gulf of Maine and Mediterranean Sea MHWs were closer to the global average duration (2.99 months) and average total area ($3.17 \times 10^8 \text{ km}^2$) of all 813 MHWs detected from September 1981 through January 2021.

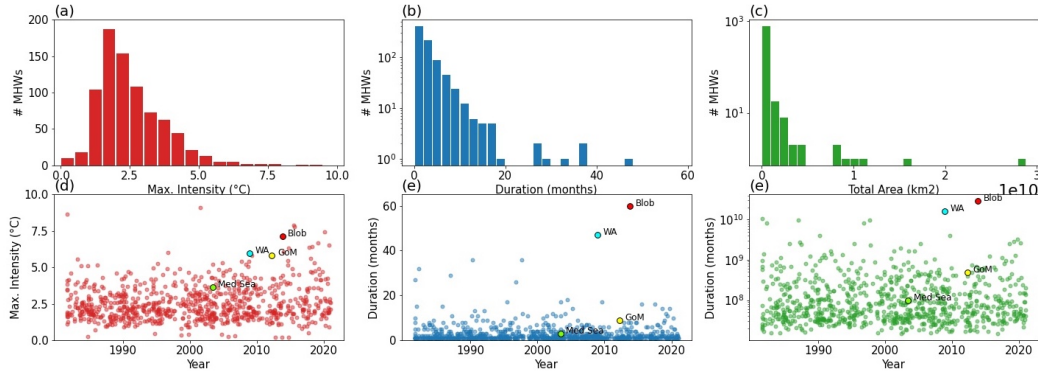


Figure 7. Distribution of (a) maximum intensity (mean= 2.55°C , min.= 0.20°C , max.= 9.11°C), (b) duration (mean=2.99 months, minimum=1 month, maximum=60 months), and (c) total area (mean= $3.17 \times 10^8 \text{ km}^2$, minimum= $1.47 \times 10^7 \text{ km}^2$, maximum= $2.88 \times 10^{10} \text{ km}^2$) for 813 MHWs detected between September 1981 through January 2021. MHWs are identified from the $1/4^\circ$ resolution OISSTv2 and defined when the detrended SST exceeds the local monthly averaged 90th percentile. MHWs have been smoothed with a 8 grid spacing morphological radius and only events that exceed the 75th percentile ($1.85 \times 10^6 \text{ km}^2$) of the initial areal distribution are considered. Named MHW are indicated by the colored dots using definitions in Table 3.

The maximum MHW intensity has a positively skewed distribution with a mean of 2.55°C , maximum of 9.11°C , and minimum of 0.20°C (Figure 7). The 2013-2017 Northeast Pacific "The Blob" had maximum SSTa of 7.13°C , which is larger than than the 2009-2011 Western Australia (5.96°C), 2012 Gulf of Maine (5.82°C), and 2003 Mediterranean Sea (3.62°C) MHWs, although the maximum intensities of all four MHWs were above average (Figure 7a, Table 3).

Measures of Table 1 are useful to describe MHWs and characterize their evolutions in both time and space. In the following section, we use Ocetrac to detect and follow four well-known MHWs occurring during the 21st century, including the 2013-2017 Northeast Pacific (Bond et al., 2015; Di Lorenzo & Mantua, 2016), 2009-2011 Western Australia (Pearce & Feng, 2013), 2012 Gulf of Maine (Mills et al., 2013), and 2003 Mediterranean Sea MHWs (Black et al., 2004; Sparnocchia et al., 2006).

Table 3. Spatiotemporal metrics using Ocetrac to describe four well-known and highly impactful 21st Century marine heatwaves.

Region	Start date	End date	Duration (months)	Intensity (Mean (°C), Max. (°C), Cumulative (°C months))	Area (km ²) (Mean, Max., Total)	Centroids Total (max. per month)
Northeast Pacific	11/2012	10/2018	60	0.98 7.13 2.82x10 ⁶	4.81x10 ⁸ 1.50x10 ⁹ 2.88x10 ¹⁰	195 (7)
Gulf of Maine	04/2012	12/2012	9	1.41 5.82 8.91x10 ⁴	5.49x10 ⁷ 1.03x10 ⁸ 4.94x10 ⁸	9 (1)
West Coast of Aus.	12/2008	10/2012	47	0.82 5.96 1.38x10 ⁶	3.45x10 ⁸ 6.98x10 ⁸ 1.62x10 ¹⁰	151 (7)
Mediterranean Sea	06/2003	08/2003	3	1.57 3.62 1.59x10 ⁴	3.30x10 ⁷ 3.76x10 ⁷ 9.90x10 ⁷	3 (1)

5 Case Studies

Ocetrac provides a global dataset of MHW spatiotemporal metrics that we can then probe to explore how past events evolved (Table 3). Here, we explore these recent events and determine (1) if their representation using Ocetrac is consistent with past literature, and (2) if there is anything new that can be learned about MHWs by taking into consideration their spatial and temporal connectivity. We focus on four events that had major impacts on both socioeconomic and ecological systems and that sample from unique geographic regions in both the tropics and mid-latitudes.

5.1 Northeast Pacific

A MHW, colloquially referred to as "The Blob," in the Northeast Pacific was notorious for its unusually large scale, its persistences magnitude of its temperature anomaly (Bond et al., 2015). MHW anomalies that developed in late 2013 were connected to the warm SSTs in the western tropical Pacific months prior through the excitement of atmospheric Rossby waves that weakened the mean state of atmospheric circulation over the North Pacific (Hartmann, 2015). This resulted in an exceptionally high ridge of atmospheric pressure through the winter of 2014 that weakened surface wind speeds, lowered rates of turbulent heat loss from the ocean to the atmosphere, and reduced the normal Ekman transport of cold water from the north (Bond et al., 2015). Offshore SST anomalies that formed during the boreal winter of 2013/14 made their way to the U.S. West Coast by late spring following the mean circulation of the ocean gyre (Di Lorenzo & Mantua, 2016). The MHW lingered for several years along the coast and was strengthened equatorward by an extreme 2015/16 El Niño in the eastern equatorial Pacific (Tseng et al., 2017). Pacific anomalies in 2013-2015 were dynamically linked through atmospheric

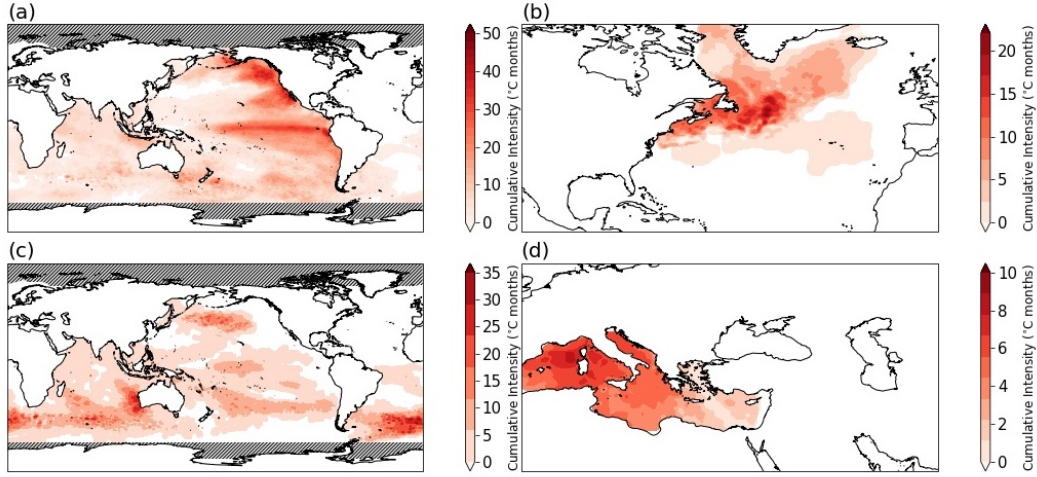


Figure 8. Spatiotemporal evolution of the cumulative intensity (°C-months) over the entire footprint of (a) the Northeast Pacific "Blob" (event #692, 11/2012 to 10/2018), (b) the Gulf of Maine (event #651, 04/2012 to 12/2012), (c) the Western Australia (event #606, 12/2008 to 10/2012) and (d) the Mediterranean Sea (#464, 06/2003 to 08/2003). Data are from the monthly $1/4^\circ$ resolution OISSTv2 with the trend removed using a minimum area threshold of the 75th percentile and an edge detection radius of 8 grid spaces (approx. 2° latitude and longitude).

variability and thermodynamic coupling that manifested on top of modes of North Pacific decadal SST variability (Tseng et al., 2017; Di Lorenzo & Mantua, 2016; Lee et al., 2015),.

We use Ocetrac to explore the spatial connectivity of Pacific anomalies during this multi-year event and track its evolution through time (Figure 8a, Supplementary 1). The entire footprint of this MHW is $2.88 \times 10^{10} \text{ km}^2$. The initial signature appeared in late 2013 just south of the Gulf of Alaska as described by Bond et al. (2015). The MHW was confined to the western and northeast Pacific through late 2014. SST anomalies in the Indian Ocean were above average for most of 2014, which played a factor in the failed development of a major El Niño event in 2014/2015 (Dong & McPhaden, 2018; McPhaden, 2015). The warm background SSTs likely enabled the MHW to grow in the Indian Ocean and persist through 2015. Meanwhile, the North Pacific portion of this mega MHW resembled the spatial pattern of the positive Pacific Decadal Oscillation (PDO) in winter 2015 that extended from the Gulf of Alaska to the eastern tropical Pacific (Supplementary 1). Di Lorenzo and Mantua (2016) showed that the weak El Niño of 2014/2015 provided the Aleutian Low with enough variability to drive this PDO-like expression of SST anomalies. This variability, along with increased heat content in the tropical Pacific, were important precursors to the development of the most powerful El Niño on record in 2015/2016. Individual snapshots of the monthly evolution of the objects contained within this event demonstrate its global reach (Supplementary 1).

5.2 Gulf of Maine

The Gulf of Maine MHW in 2012 covered an ocean area from Cape Hatteras, North Carolina to Iceland and up into the Labrador Sea (Figure 8b; Mills et al., 2013). A northward meridional shift in the atmospheric jet stream over North America during the late autumn and early winters of 2011/2012 stabilized atmospheric high pressure over the western North Atlantic (Chen et al., 2014). This led to an overall reduction in surface wind

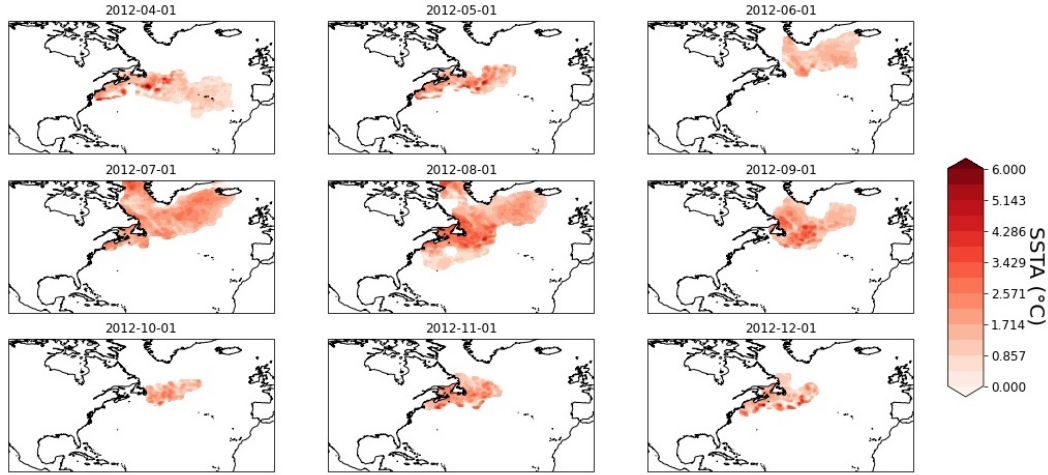


Figure 9. Spatiotemporal evolution of the SSTa (°C) over the entire footprint of the Gulf of Maine (event #651).

speeds and higher than normal air humidity and temperature, which acted to inhibit turbulent heat loss from the ocean to the atmosphere and increase water column stratification (Chen et al., 2014). As a result, SSTs systematically warmed over the continental shelf from November 2011 through at least June 2012 (Chen et al., 2014). Anomalous warming in the spring of 2012 was attributed to large-scale atmospheric variability during the winter of 2011/2012, whereas local advective heat flux played a secondary role to cool SSTs (Chen et al., 2014, 2015).

The results from Ocetrac show that the Gulf of Maine MHW a regional event that was confined to the Northwest Atlantic. The center of action was centered offshore of Newfoundland with maximum cumulative intensities occurring in the Gulf of Maine, Gulf of St. Lawrence, and part of the Labrador Sea (Figure 7b). The MHW, which began in April 2012, persisted for 9 months and covered a total ocean area of $6.67 \times 10^7 \text{ km}^2$ with a maximum intensity of 5.82°C (Table 3).

Scannell et al. (2016) also tracked the 2012 Gulf of Maine MHW using 2° -latitude by 2° -longitude resolution monthly detrended SST for three months, between June and August 2012, and found its area to be $7.60 \times 10^6 \text{ km}^2$ with a maximum intensity exceed 3°C . They also showed that the likelihood of a MHW this size is enhanced during the negative phase of the North Atlantic Oscillation (NAO) and positive phase of the Atlantic Multidecadal Oscillation (AMO), with the AMO being more dominant. Unsurprisingly, the AMO had been positive since the early 1990s and the NAO took a negative excursion in 2012. The resulting relationship between natural modes of SST variability and MHW size may have favored the large-scale nature of the 2012 warm anomalies (Supplementary 2).

5.3 West Coast of Australia

A major, unprecedented MHW occurred in late February 2011 off the coast of Western Australia (Pearce & Feng, 2013). An important driver of this MHW was the fast phase transition from Central Pacific El Niño in 2009/2010 to La Niña in 2010/2011 that was in part driven by strong easterly wind stress caused by warm SSTs in the Indian Ocean (Kim et al., 2011). Easterly wind anomalies in the western Tropical Pacific and over Indonesia excited an eastward upwelling Kelvin wave that quickly terminated warming as-

sociated with an el Niño in 2009/2010 (Kim et al., 2011; Kug & Kang, 2006; Yoo et al., 2010). An extraordinary La Niña quickly ensued, which increased SSTs and sea level heights in the western tropical Pacific and off the northwest coast of Australia. High steric height anomalies forced a stronger than normal poleward flowing Leeuwin Current (Feng et al., 2013). In addition, northerly wind anomalies associated with low sea level pressure anomalies off the coast of Western Australia helped to intensify the Leeuwin Current and reduce turbulent heat loss from the ocean (Feng et al., 2013). The poleward advection of warm water contributed to two thirds of the warming, while positive air-sea heat fluxes into the ocean accounted for approximately the other one third of the warming (J. A. Benthuisen et al., 2020). The anomalous air-sea heat flux in February 2011 acted to reinforce the MHW rather than damp the warming effects from La Niña (Feng et al., 2013). The exceptional MHW that resulted along Australia’s western coast was dubbed ‘Ningaloo Niño’ for its semblance to other coupled ocean-atmosphere phenomena in the Pacific (El Niño) and Atlantic (Benguela Niño) (Feng et al., 2013). After the peak warming in March 2011 along the coast, positive sea level and SST anomalies propagated offshore following the propagation of mesoscale eddies (J. Benthuisen et al., 2014).

Indian Ocean SSTs during the following summers of 2012 and 2013 remained anomalously warm off Western Australia (Caputi et al., 2014) (Supplementary 3). The persistence of anomalies was part of an increasing trend of Ningaloo Niño conditions since the early 1990s (Feng et al., 2013). The trend was driven in part by a change to the negative phase of the Interdecadal Pacific Oscillation (IPO) and enhanced ENSO variance, the former sustains positive heat content anomalies off Western Australia and favors cyclonic wind anomalies that reduce the prevailing alongshore southerly winds and enhance poleward heat transport by the Leeuwin Current (Feng et al., 2013). Further coupling between the along-shore winds and coastal SST has been shown to amplify Ningaloo Niño events (Kataoka et al., 2014).

5.4 Mediterranean Sea

During the summer of 2003, Western Europe experience its worst heatwave in over 500 years, which caused excessive morbidity throughout the region, especially in hard hit France (Luterbacher et al., 2004; Valleron & Boumendil, 2004). The extremely hot conditions over land from May through August stemmed from a persistent anticyclonic circulation centered over northern France that reduced cloud cover and precipitation (Black et al., 2004; Grazzini & Viterbo, 2003). Although short-lived, the anomalous atmospheric anomalies quickly warmed SSTs in the central Mediterranean Sea in May before affecting the entire basin by July, with the exception of the Aegean Sea (Grazzini & Viterbo, 2003). The Mediterranean Sea MHW warmed passively as a result of increased surface air temperatures, reduced surface wind speeds, and lower rates of turbulent and long-wave heat loss to the atmosphere (Olita et al., 2006). The MHW dissipated abruptly in late August to early September when strong westerly winds cooled surface air temperatures and induced wind-driven turbulent mixing that cooled SSTs (Sparnocchia et al., 2006).

The Mediterranean Sea MHW in Ocetrac during the summer of 2003 started in June and persisted through August (Supplementary 4). Due to the nature of the semi-enclosed region, MHW anomalies in the Mediterranean Sea did not connect with those in the Atlantic and had only one centroid per month. This meant that the MHW was highly localized with maximum anomalies over 4°C and a total surface area of $7.76 \times 10^6 \text{ km}^2$, where the maximum cumulative anomalies occurred in the central and western regions of the basin (Table 3, Figure 8d). The 2003 Mediterranean Sea MHW was the smallest size event of the four case studies examined here, however, was intense enough to decimate rocky benthic macroinvertebrate species (Table 3; Garrabou et al., 2009).

Remote forcing from the northward shift and intensification of the Inter-tropical Convergence Zone over West Africa, as well as Rossby waves emanating from tropical America that intensified the Azores anticyclone, contributed to the unusual atmospheric conditions driving the 2003 Mediterranean Sea MHW (Black et al., 2004). Decadal fluctuations in North Atlantic SSTs and the thermohaline circulation are known to influence European weather over long timescales. During 2003, the AMO index was positive and associated with elevated air temperatures and reduced wind stress over western Europe (Sutton & Hodson, 2005).

6 Conclusions

We present a novel tracking algorithm called Ocetrac that can be used to characterize the spatiotemporal evolution of MHWs globally. This new software tool has allowed us to highlight the spatial connectivity and temporal behavior of MHWs. Using Ocetrac, we are able to characterize new spatial patterns and behavior of some of the most dangerous MHWs of the 21st century. A summary of our approach is as follows:

1. **Proprocess** global SSTs to exclude the long-term warming trend and define anomalies with respect to the local climatology. Anomalies are then standardized by the monthly standard deviation of SSTa over the entire climatological period. The climatological periods should cover at least the most recent 30-years.
2. **Detect** MHWs where SSTa exceed a local seasonally varying threshold (e.g., 90th percentile) computed over the same climatological period. Connect edges that define the perimeter of MHWs larger than a minimum size threshold (e.g., 75th percentile of the anomaly size distribution).
3. **Track** MHWs using 3D connectivity in both space (x, y) and time (z) keeping track of multiple centroids as MHWs split or merge.

We demonstrate the usefulness of Ocetrac in following the evolutions of four well-known MHWs in the Pacific, Indian, and Atlantic Oceans, and Mediterranean Sea. The advantage of using Ocetrac globally, rather than a single regionally focused analysis, is that it captures the large-scale and dynamically linked connections between remote SST anomalies that connect seemingly disconnected MHWs. In combination with dynamical studies, Ocetrac can provide a tool to better understand the origin of MHWs and their evolution.

To a large extent, our interpretation of extreme events is dependent on how thresholds are defined. In many circumstances, extreme events are determined based on the space and time scales of their impacts and associated risks. For example, extreme flooding events are often classified by their extent and frequency in terms of their potential for damage (Ten Veldhuis, 2011). It is therefore useful to consider MHWs as temperature variance outside the normal range of thermal tolerance to native species. However, here, we remove the long term warming trend in order to better isolate the behavior of SST variance to be able to describe the spatiotemporal connectedness of MHWs. However, when we retain the long-term warming trend, a greater proportion of ocean surface area experiences a MHW, and thus leads to increases in intensity, duration, and size.

We also explore the sensitivity of Ocetrac to the resolution of gridded observational data, ranging from eddy-permitting (0.25°) to very coarse (2°). The overall large-scale spatial patterns agree well among the different resolutions, however the MHWs tracked with coarser resolution lacked the intensity and frequency expected with higher resolution. These results are consistent with modeling studies (Hayashida et al., 2020; Pilo et al., 2019), and agree that greater spatial detail gained from high resolution datasets better represent the changes expected to occur to MHWs in the future. The inclusion of high-quality, near real time data remains a challenge for making up-to-date and accurate fore-

casts (Schlegel et al., 2019). However, visualizing and quantifying the spatiotemporal connectivity of MHWs in sea surface temperature forecasts using Ocetrac enhanced the usability of sea surface temperature forecasts.

Open Research Section

The NOAA OISSTv2 dataset was provided by the NOAA/OAR/ESRL PSL, Boulder, Colorado, USA, from their website at <https://psl.noaa.gov/> and used in the creation of this manuscript. Figures were made with Matplotlib version 3.5.2 (Caswell et al., 2020; Hunter, 2007), available under the Matplotlib license at <https://matplotlib.org/>. Ocetrac, the software associated with this manuscript for tracking the spatiotemporal evolution of marine heatwaves is licensed under MIT and published on GitHub <https://github.com/ocetrac/ocetrac/> (Scannell, Hillary and Busecke, Julius and Abernathey, Ryan, and Gagne, David John, and Thompson, LuAnne, and Whitt, Daniel, 2021). The data processing, figures, and calculations associated with this manuscript is published on Github <https://github.com/CassiaCai/spatiotemp-evolution-of-mhws-globally>.

Acknowledgments

HAS and LT are supported by an AI for Earth Innovation Grant sponsored by the Leonardo DiCaprio Foundation and Microsoft, and wish to acknowledge cloud resources from an Azure compute grant awarded through Microsoft’s AI for Earth. HAS and RPA received support from the Gordon and Betty Moore Foundation.

References

- Amaya, D. J., Miller, A. J., Xie, S.-P., & Kosaka, Y. (2020). Physical drivers of the summer 2019 north pacific marine heatwave. *Nature communications*, 11(1), 1903.
- Benthuisen, J., Feng, M., & Zhong, L. (2014). Spatial patterns of warming off western australia during the 2011 ningaloo niño: Quantifying impacts of remote and local forcing. *Continental Shelf Research*, 91, 232–246.
- Benthuisen, J. A., Oliver, E. C., Chen, K., & Wernberg, T. (2020). Advances in understanding marine heatwaves and their impacts. *Frontiers in Marine Science*, 147.
- Black, E., Blackburn, M., Harrison, G., Hoskins, B., Methven, J., et al. (2004). Factors contributing to the summer 2003 european heatwave. *Weather*, 59(8), 217–223.
- Bond, N. A., Cronin, M. F., Freeland, H., & Mantua, N. (2015). Causes and impacts of the 2014 warm anomaly in the ne pacific. *Geophysical Research Letters*, 42(9), 3414–3420.
- Caputi, N., Jackson, G., & Pearce, A. (2014). The marine heat wave off western australia during the summer of 2010/11–2 years on.
- Chen, K., Gawarkiewicz, G., Kwon, Y.-O., & Zhang, W. G. (2015). The role of atmospheric forcing versus ocean advection during the extreme warming of the northeast us continental shelf in 2012. *Journal of Geophysical Research: Oceans*, 120(6), 4324–4339.
- Chen, K., Gawarkiewicz, G. G., Lentz, S. J., & Bane, J. M. (2014). Diagnosing the warming of the northeastern us coastal ocean in 2012: A linkage between the atmospheric jet stream variability and ocean response. *Journal of Geophysical Research: Oceans*, 119(1), 218–227.
- Cheung, W. W., & Frölicher, T. L. (2020). Marine heatwaves exacerbate climate change impacts for fisheries in the northeast pacific. *Scientific reports*, 10(1), 1–10.
- Darmaraki, S., Somot, S., Sevault, F., & Nabat, P. (2019). Past variability of

- mediterranean sea marine heatwaves. *Geophysical Research Letters*, 46(16), 9813–9823.
- Di Lorenzo, E., & Mantua, N. (2016). Multi-year persistence of the 2014/15 north pacific marine heatwave. *Nature Climate Change*, 6(11), 1042–1047.
- Dong, L., & McPhaden, M. J. (2018). Unusually warm indian ocean sea surface temperatures help to arrest development of el niño in 2014. *Scientific reports*, 8(1), 2249.
- Eakin, C. M., Morgan, J. A., Heron, S. F., Smith, T. B., Liu, G., Alvarez-Filip, L., ... others (2010). Caribbean corals in crisis: record thermal stress, bleaching, and mortality in 2005. *PloS one*, 5(11), e13969.
- Feng, M., McPhaden, M. J., Xie, S.-P., & Hafner, J. (2013). La niña forces unprecedented leeuwine current warming in 2011. *Scientific reports*, 3(1), 1277.
- Fewings, M. R., & Brown, K. S. (2019). Regional structure in the marine heat wave of summer 2015 off the western united states. *Frontiers in Marine Science*, 6, 564.
- Frölicher, T. L., Fischer, E. M., & Gruber, N. (2018). Marine heatwaves under global warming. *Nature*, 560(7718), 360–364.
- Gagne, D. J., McGovern, A., Haupt, S. E., Sobash, R. A., Williams, J. K., & Xue, M. (2017). Storm-based probabilistic hail forecasting with machine learning applied to convection-allowing ensembles. *Weather and forecasting*, 32(5), 1819–1840.
- Garrahou, J., Coma, R., Bensoussan, N., Bally, M., Chevaldonné, P., Cigliano, M., ... others (2009). Mass mortality in northwestern mediterranean rocky benthic communities: effects of the 2003 heat wave. *Global change biology*, 15(5), 1090–1103.
- Gonzalez, R. C., & Woods, R. E. (2002). *Digital image processing* (2nd ed.). Upper Saddle River, NJ: Prentice Hall.
- Grazzini, F., & Viterbo, P. (2003). Record-breaking warm sea surface temperature of the mediterranean sea. *ECMWF Newsletter*, 98, 30–31.
- Hartmann, D. L. (2015). Pacific sea surface temperature and the winter of 2014. *Geophysical Research Letters*, 42(6), 1894–1902.
- Hayashida, H., Matear, R. J., Strutton, P. G., & Zhang, X. (2020). Insights into projected changes in marine heatwaves from a high-resolution ocean circulation model. *Nature communications*, 11(1), 4352.
- Hobday, A. J., Alexander, L. V., Perkins, S. E., Smale, D. A., Straub, S. C., Oliver, E. C., ... others (2016). A hierarchical approach to defining marine heatwaves. *Progress in Oceanography*, 141, 227–238.
- Hobday, A. J., Oliver, E. C., Gupta, A. S., Benthuisen, J. A., Burrows, M. T., Donat, M. G., ... others (2018). Categorizing and naming marine heatwaves. *Oceanography*, 31(2), 162–173.
- Holbrook, N. J., Scannell, H. A., Sen Gupta, A., Benthuisen, J. A., Feng, M., Oliver, E. C., ... others (2019). A global assessment of marine heatwaves and their drivers. *Nature communications*, 10(1), 2624.
- Hughes, T. P., Kerry, J. T., Álvarez-Noriega, M., Álvarez-Romero, J. G., Anderson, K. D., Baird, A. H., ... others (2017). Global warming and recurrent mass bleaching of corals. *Nature*, 543(7645), 373–377.
- Kataoka, T., Tozuka, T., Behera, S., & Yamagata, T. (2014). On the ningaloo niño/niña. *Climate dynamics*, 43, 1463–1482.
- Kayanne, H. (2017). Validation of degree heating weeks as a coral bleaching index in the northwestern pacific. *Coral Reefs*, 36(1), 63–70.
- Kim, W., Yeh, S.-W., Kim, J.-H., Kug, J.-S., & Kwon, M. (2011). The unique 2009–2010 el niño event: A fast phase transition of warm pool el niño to la niña. *Geophysical Research Letters*, 38(15).
- Kug, J.-S., & Kang, I.-S. (2006). Interactive feedback between enso and the indian ocean. *Journal of climate*, 19(9), 1784–1801.

- Lakshmanan, V., Hondl, K., & Rabin, R. (2009). An efficient, general-purpose technique for identifying storm cells in geospatial images. *Journal of Atmospheric and Oceanic Technology*, 26(3), 523–537.
- Lee, M.-Y., Hong, C.-C., & Hsu, H.-H. (2015). Compounding effects of warm sea surface temperature and reduced sea ice on the extreme circulation over the extratropical north pacific and north america during the 2013–2014 boreal winter. *Geophysical Research Letters*, 42(5), 1612–1618.
- Luterbacher, J., Dietrich, D., Xoplaki, E., Grosjean, M., & Wanner, H. (2004). European seasonal and annual temperature variability, trends, and extremes since 1500. *Science*, 303(5663), 1499–1503.
- McCabe, R. M., Hickey, B. M., Kudela, R. M., Lefebvre, K. A., Adams, N. G., Bill, B. D., ... Trainer, V. L. (2016). An unprecedented coastwide toxic algal bloom linked to anomalous ocean conditions. *Geophysical Research Letters*, 43(19), 10–366.
- McKinnon, K. A., & Deser, C. (2018). Internal variability and regional climate trends in an observational large ensemble. *Journal of Climate*, 31(17), 6783–6802.
- McPhaden, M. J. (2015). Playing hide and seek with el niño. *Nature Climate Change*, 5(9), 791–795.
- Mills, K. E., Pershing, A. J., Brown, C. J., Chen, Y., Chiang, F.-S., Holland, D. S., ... others (2013). Fisheries management in a changing climate: lessons from the 2012 ocean heat wave in the northwest atlantic. *Oceanography*, 26(2), 191–195.
- Olita, A., Sorgente, R., Ribotti, A., Natale, S., et al. (2006). Effects of the 2003 european heatwave on the central mediterranean sea surface layer: a numerical simulation. *Ocean Science Discussions*, 3(3), 85–125.
- Oliver, E. C., Benthuyssen, J. A., Bindoff, N. L., Hobday, A. J., Holbrook, N. J., Mundy, C. N., & Perkins-Kirkpatrick, S. E. (2017). The unprecedented 2015/16 tasman sea marine heatwave. *Nature communications*, 8(1), 16101.
- Oliver, E. C., Donat, M. G., Burrows, M. T., Moore, P. J., Smale, D. A., Alexander, L. V., ... others (2018). Longer and more frequent marine heatwaves over the past century. *Nature communications*, 9(1), 1–12.
- Pearce, A. F., & Feng, M. (2013). The rise and fall of the “marine heat wave” off western australia during the summer of 2010/2011. *Journal of Marine Systems*, 111, 139–156.
- Perkins-Kirkpatrick, S., King, A. D., Cougnon, E., Grose, M. R., Oliver, E., Holbrook, N., ... others (2019). The role of natural variability and anthropogenic climate change in the 2017/18 tasman sea marine heatwave.
- Pershing, A. J., Record, N. R., Franklin, B. S., Kennedy, B. T., McClenachan, L., Mills, K. E., ... Wolff, N. H. (2019). Challenges to natural and human communities from surprising ocean temperatures. *Proceedings of the National Academy of Sciences*, 116(37), 18378–18383.
- Pilo, G. S., Holbrook, N. J., Kiss, A. E., & Hogg, A. M. (2019). Sensitivity of marine heatwave metrics to ocean model resolution. *Geophysical Research Letters*, 46(24), 14604–14612.
- Power, S., Casey, T., Folland, C., Colman, A., & Mehta, V. (1999). Inter-decadal modulation of the impact of enso on australia. *Climate dynamics*, 15, 319–324.
- Reynolds, R. W., Rayner, N. A., Smith, T. M., Stokes, D. C., & Wang, W. (2002). An improved in situ and satellite sst analysis for climate. *Journal of climate*, 15(13), 1609–1625.
- Reynolds, R. W., Smith, T. M., Liu, C., Chelton, D. B., Casey, K. S., & Schlax, M. G. (2007). Daily high-resolution-blended analyses for sea surface temperature. *Journal of climate*, 20(22), 5473–5496.
- Rodriguez, S. P. (2021). The impact of drought on agriculture in new mexico.

- Scannell, H. A., Pershing, A. J., Alexander, M. A., Thomas, A. C., & Mills, K. E. (2016). Frequency of marine heatwaves in the north atlantic and north pacific since 1950. *Geophysical Research Letters*, *43*(5), 2069–2076.
- Scannell, Hillary and Busecke, Julius and Abernathey, Ryan, and Gagne, David John, and Thompson, LuAnne, and Whitt, Daniel. (2021). *ocetrac*. [Software] Available at <https://github.com/ocetrac/ocetrac>. GitHub. Accessed on July 19, 2023.
- Schlegel, R. W., Oliver, E. C., Hobday, A. J., & Smit, A. J. (2019). Detecting marine heatwaves with sub-optimal data. *Frontiers in Marine Science*, *6*, 737.
- Sen Gupta, A., Thomsen, M., Benthuyzen, J. A., Hobday, A. J., Oliver, E., Alexander, L. V., ... others (2020). Drivers and impacts of the most extreme marine heatwave events. *Scientific reports*, *10*(1), 19359.
- Smale, D. S., Wernberg, T., Oliver, E. C. J., Thomsen, M., Harvey, B. P., Straub, S. C., ... Moore, P. J. (2019). Marine heatwaves threaten global biodiversity and the provision of ecosystem services. *Nature Climate Change*, *9*, 306–312.
- Sparnocchia, S., Schiano, M., Picco, P., Bozzano, R., & Cappelletti, A. (2006). The anomalous warming of summer 2003 in the surface layer of the central ligurian sea (western mediterranean). In *Annales geophysicae* (Vol. 24, pp. 443–452).
- Sun, D., Jing, Z., Li, F., & Wu, L. (2023). Characterizing global marine heatwaves under a spatio-temporal framework. *Progress in Oceanography*, *211*, 102947.
- Sutton, R. T., & Hodson, D. L. (2005). Atlantic ocean forcing of north american and european summer climate. *science*, *309*(5731), 115–118.
- Ten Veldhuis, J. (2011). How the choice of flood damage metrics influences urban flood risk assessment. *Journal of Flood Risk Management*, *4*(4), 281–287.
- Tseng, Y.-H., Ding, R., & Huang, X.-m. (2017). The warm blob in the northeast pacific—the bridge leading to the 2015/16 el niño. *Environmental Research Letters*, *12*(5), 054019.
- Valleron, A.-J., & Boumendil, A. (2004). Epidemiology and heat waves: analysis of the 2003 episode in france. *Comptes rendus biologiques*, *327*(12), 1125–1141.
- Williams, A. P., Seager, R., Abatzoglou, J. T., Cook, B. I., Smerdon, J. E., & Cook, E. R. (2015). Contribution of anthropogenic warming to california drought during 2012–2014. *Geophysical Research Letters*, *42*(16), 6819–6828.
- Xu, J., Lowe, R. J., Ivey, G. N., Jones, N. L., & Zhang, Z. (2018). Contrasting heat budget dynamics during two la nina marine heat wave events along northwestern australia. *Journal of Geophysical Research: Oceans*, *123*(2), 1563–1581.
- Yoo, S.-H., Fasullo, J., Yang, S., & Ho, C.-H. (2010). On the relationship between indian ocean sea surface temperature and the transition from el niño to la niña. *Journal of Geophysical Research: Atmospheres*, *115*(D15).